Formation Mechanism and Properties of CdS-Ag_2S Nanorod Superlattices

Denis O. Demchenko,[†,*] Richard D. Robinson,[‡] Bryce Sadtler,[‡,§] Can K. Erdonmez,[§] A. Paul Alivisatos,[‡,§] and Lin-Wang Wang[†]

[†]Computational Research Division, Lawrence Berkeley National Laboratory, Berkeley, California 94720, [‡]Materials Science Division, Lawrence Berkeley National Laboratory, Berkeley, California 94720, and [§]Department of Chemistry, University of California, Berkeley, California 94720

ABSTRACT The mechanism of formation of recently fabricated CdS-Ag_2S nanorod superlattices is considered and their elastic properties are predicted theoretically based on experimental structural data. We consider different possible mechanisms for the spontaneous ordering observed in these 1D nanostructures, such as diffusion-limited growth and ordering due to epitaxial strain. A simplified model suggests that diffusion-limited growth partially contributes to the observed ordering, but cannot account for the full extent of the ordering alone. The elastic properties of bulk Ag_2S are predicted using a first principles method and are fed into a classical valence force field (VFF) model of the nanostructure. The VFF results show significant repulsion between Ag_2S segments, strongly suggesting that the interplay between the chemical interface energy and strain due to the lattice mismatch between the two materials drives the spontaneous pattern formation.

KEYWORDS: nanorod superlattices · CdS-Ag_2S · strain · ordering · cation exchange

There has been much recent progress in fabricating one-dimensional (1D) superlattices (*e.g.*, Si/SiGe,[1] InAs/InP,[2] and GaAs/GaP[3] superlattice nanowires), stimulated by the interest in the use of such nanostructures in photonic and thermoelectric applications. The vapor–liquid–solid (VLS) methods typically employed to grow these structures are facile but often yield large feature sizes.[1–3] Adoption of colloidal methods for nanostructure fabrication has the potential advantages of lower costs and achievement of smaller structures with enhanced and tunable quantum confinement effects that can be utilized in optoelectronic devices such as light-emitting diodes and solar cells.[4,5] However, to date, published preparations of 1D superlattices using colloidal growth[6] have been cumbersome with the resulting 1D superlattices, which have only a few layers before the procedure is too difficult.[7] An alternative to this method would be to develop a spontaneous ordering method, where a pattern of nanostructures emerges naturally due to intrinsic interactions on the nanoscale. For instance, in growth of 2D and 3D structures, lattice strain has been used to drive pattern formation on the nanoscale, yielding self-assembled quantum dots and their ordered arrays following epitaxial growth.[8–13] In these experiments, strain fields created by lattice mismatch between the deposited quantum dots (QD) and the substrate (or the overlayer) influence the deposition of subsequent QD layers, leading to formation of vertically ordered QD arrays. Another source of spontaneous pattern formation in semiconductor nanostructures is diffusion-limited ordering,[14] where, in principle, a regular pattern can form due to slow diffusion of atoms between growing islands.

We recently showed that partial cation exchange can be used to introduce ordered Ag_2S segments into CdS nanorods.[15] During cation exchange, dissolved Ag^+ ions displace Cd^{2+} cations from CdS nanorods also present in solution, resulting in islands of Ag_2S in the CdS nanorods. As the reaction progresses, the growing Ag_2S islands yield segments which are arranged periodically within the nanorod. A transmission electron microscopy (TEM) image of such nanorod superlattices is shown in Figure 1a, where a periodic arrangement of the dark Ag_2S segments within the nanorods is visible. If an excess of Ag^+ cations are added, eventually the whole CdS nanorod converts into a Ag_2S nanorod, preserving shape and length. If however, only a partial cation exchange is performed, the nanorod superlattices are formed and remain stable, dried on a substrate for months. We hypothesized the formation of such spontaneously ordered superlattices to be driven largely by the lattice strain field created at the CdS-Ag_2S interfaces (see ref 15 for an introduction and brief discussion of these ideas). The strain fields are expected to result in repulsion between Ag_2S segments, which,

*Address correspondence to dodemchenko@lbl.gov.

Received for review November 21, 2007 and accepted March 06, 2008.

Published online April 5, 2008.
10.1021/nn700381y CCC: $40.75

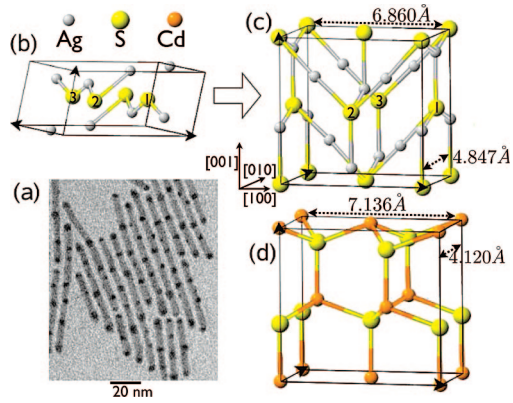

Figure 1. (a) Experimental TEM image of CdS-Ag_2S nanorod superlattices fabricated by partial cation exchange. The dark regions are the Ag_2S segments embedded in the CdS nanorods. (b) Monoclinic phase of Ag_2S unit cell matching the experimental XRD data (corresponding to Table 1). (c) Orthorhombic Ag_2S supercell, built from monoclinic unit cells (see also Table 1) (b), used to epitaxially attach to wurtzite CdS in the [0001] direction (d). The numbered atoms in structures b and c show the construction of the orthorhombic cell from the monoclinic unit cell. To epitaxially attach the two lattices, both CdS and Ag_2S must distort. The lattice mismatch between wurtzite CdS and the orthorhombic supercell of Ag_2S is +4% tension along the [100] Ag_2S supercell axis ([1000] wurtzite) and −15% compression along the [010] Ag_2S supercell axis ([2100] wurtzite). This creates a large strain when both lattices distort, relaxing into the lowest energy geometry.

operating in concert with diffusion-limited Ostwald ripening, can yield and stabilize the observed periodic patterns. In this paper, we present more detailed theoretical considerations of the mechanism of formation as well as the structural and elastic properties of the CdS nanorod superlattices.

RESULTS AND DISCUSSION

An Overview of Formation of CdS-Ag_2S Nanorod Superlattice. In the partial cation exchange experiments, the initial colloidal CdS nanorods are fabricated to be very smooth with small diameter dispersion (about 10%) and with lengths ranging between 30 and 100 nm. The colloidal CdS nanorods are added to a solution of toluene, $AgNO_3$, and methanol at −66 °C in air.[15] During the cation exchange reaction, the Ag^+ cations substitute for Cd^{2+} cations within the nanorods, owing to the preferential binding of methanol to the divalent Cd^{2+} ion over Ag^+.[16] This solid-state exchange reaction has been shown to take place on a millisecond time scale on the nanoscale because of the small size of the nanocrystals and the high mobility of Ag^+ and Cd^{2+} within the crystalline lattices.[16,17] The process is facilitated by the fact that both Ag^+ and Cd^{2+} are fast diffusers in CdS.[18,19] The concentration of $AgNO_3$ controls the number of Ag^+ cations and therefore defines the fraction of Cd^{2+} cations to be exchanged: an excess of Ag^+ cations results in complete conversion of the CdS rods into Ag_2S.[16] At low Ag^+ concentrations, the resulting partial cation exchange reaction produces a random arrangement of Ag_2S islands embedded in the nanorod surfaces. At intermediate Ag^+ concentrations, the islands appear to have grown larger and have intercalated into the nanorod interior, owing to the additional Ag^+ cations as well as the absorption of smaller islands by larger ones (Ostwald ripening).

TABLE 1. Crystal Data for the Monoclinic Phase of Ag_2S[a]

Lattice Parameters (in Å) and Angle			
a	b	c	β
4.231	6.93	9.526	125.29°
Atomic Positions			
atom	x	y	z
S	0.5	0.7383	0.3694
S	0.5	0.7617	0.8694
S	0.5	0.2617	0.6306
S	0.5	0.2383	0.1306
Ag	0.0712	0.0169	0.3075
Ag	0.7259	0.3213	0.4362
Ag	0.9288	0.5169	0.1925
Ag	0.9288	0.9831	0.6925
Ag	0.0712	0.4831	0.8075
Ag	0.2741	0.8213	0.0638
Ag	0.2741	0.6787	0.5638
Ag	0.7259	0.1787	0.9362

[a]The modeled XRD pattern for this structure matches the experimental XRD pattern of Ag_2S segments in the CdS-Ag_2S nanorod superlattices. The monoclinic unit cell axes are related to the orthorhombic supercell as $a = [0, -0.5, 0.5]$, $b = [100]$, $c = [020]$.

As the islands grow, they will eventually span the entire nanorod diameter, achieving a cylindrical, low interface energy geometry. This arrangement is expected to be quite stable since further diffusion of Ag^+ ions between segments will not decrease the interface area unless a whole segment is absorbed by the other segments. However, at this point, the elastic repulsion between segments is expected to stabilize the islands against further ripening, as discussed below. As a result of the ripening process, the Ag_2S segments have become spaced out within the nanorod. Furthermore, spontaneous self-ordering is facilitated by the fast diffusion of Ag^+ in the lattice, allowing for the mobile segments to make final rearrangements to minimize the repulsive strain interaction. The strain interaction is minimized when the Ag_2S segments are spaced evenly within the CdS nanorod. Thus the periodicity of the CdS-Ag_2S superlattices depends on both the dimensions of the nanorod and the number of Ag_2S regions which it contains. Thus, the periodic pattern of Ag_2S segments in the CdS nanorod (Figure 1a) results from a sequence of initial nucleation and ripening followed by elastically driven local ordering of Ag_2S segments.

CdS-Ag_2S Epitaxial Attachment. The experimental powder X-ray diffraction (XRD) patterns reveal the superlattices to contain crystalline regions of CdS (of the

wurtzite form) and Ag_2S (of the monoclinic form). The unit cell of the latter structure is shown in the Figure 1b. This monoclinic (low temperature) phase of Ag_2S has been studied in the literature[20–22] both theoretically and experimentally. It has been found to be a semiconductor with a measured bandgap ranging from 0.78 to 1.0 eV.[22] The sulfur atoms in bulk Ag_2S form a slightly distorted bcc lattice with the silver atoms occupying octahedral and tetrahedral sites of the sulfur lattice.[21] Considering the high mobility of Ag^+ ions, considerable distortions and cation disorder may be present in the highly strained and high surface area nanorod superlattices, with reference to the bulk structure.

The fully formed nanorod superlattices exhibit epitaxial attachment of Ag_2S and CdS regions. However, epitaxially attaching monoclinic Ag_2S to the CdS wurtzite lattice, along the [0001] axis of the nanorod requires significant distortions. Since the sulfur atoms in Ag_2S form a bcc lattice, we can construct a supercell (Figure 1c) directly from the original monoclinic Ag_2S unit cell (Figure 1b), where the sulfur atoms corresponding to each other in the two lattices are numbered. Explicitly, the monoclinic unit cell axes *a*, *b*, *c* are related to the orthorhombic supercell as $a = [0, -0.5, 0.5]$, $b = [100]$, $c = [020]$. This supercell (see Figure1c,d) can attach its (001) plane (which is the (110) plane of a bcc lattice) or (100) plane (which is the $(1\bar{1}0)$ plane of a bcc lattice) to the (0001) wurtzite plane of CdS (Figure 1d), since all of them have hexagonal symmetry. Such attachment however causes large distortions of both the Ag_2S and CdS lattices: namely, the Ag_2S lattice constant, in comparison with that of CdS, is 4% smaller along the [100] or [001] supercell axes ([1000] wurtzite) and 15% larger along the [010] supercell axis ([2100] wurtzite). Nevertheless, as noted before,[23,24] high strains in one-dimensional superlattices can exist without resulting in dislocation formation.

The large strains are likely a key requirement for the formation of the periodic pattern observed in nanorod superlattices. As we show here, the strain fields created by this lattice mismatch at the interface lead to a repulsive interaction between adjacent Ag_2S segments. This repulsion, coupled with the segments' mobility leads to ordering of segments and stabilization of the structure.

To confirm the crystal structure we have simulated the XRD pattern expected from a powder mixture of Ag_2S nanocubes and CdS nanorods. Several nanorod and nanocube sizes were considered to verify that the simulation provides the correct pattern for the Ag_2S size, matching the experimentally determined Ag_2S size from TEM. In Figure 2, we show the measured XRD spectrum (Figure 2a) along with the patterns computed for 5.3×11 nm CdS nanorods and Ag_2S cubes with sides of 10×10 nm, 5×5 nm, and 2.5×2.5 nm (Figure 2b,c,d, respectively). For a given geometry, all pairwise

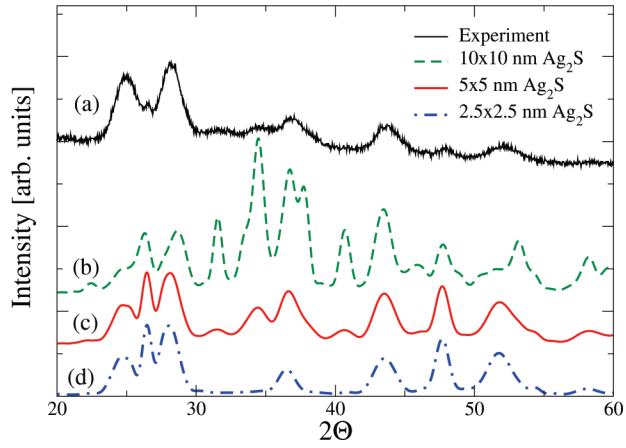

Figure 2. The experimental XRD diffraction pattern from the CdS-Ag_2S nanorod superlattices (black line) and three simulated XRD patterns. The simulated patterns are obtained by summing the pattern predicted for 5.3×11 nm CdS nanorods with the predicted pattern for Ag_2S cubes with sides of 5×5 nm (thick red line), 10×10 nm (dashed green line), and 2.5×2.5 nm (dash-dotted blue line). The simulation is performed for the Ag_2S structure described in Table 1 and Figure 1b. The result for 5×5 nm Ag_2S cubes qualitatively matches the experimental pattern. The Ag_2S peaks are broader in the experimental data because of the presence of strain created by the CdS-Ag_2S interfaces.

atomic distances, r_{ij}, were computed. Then, the XRD intensity pattern can be obtained as

$$I(S) \propto \frac{F_i(S)F_j(S)}{S} \sum_{i \neq j} \frac{\sin(2\pi r_{ij} S)}{r_{ij}} \qquad (1)$$

where, $S = 2\sin(\Theta)/\lambda$ is a scattering parameter, $I(S)$ is the computed intensity, Θ is the angle of diffraction, λ is the wavelength of incident X-rays, and $F_k(S)$ is the atomic structure factor for the *k*th atom in the nanostructure. We find a good qualitative agreement with the experimental pattern for the wurtzite structure of CdS, and the monoclinic structure of Ag_2S listed in Table 1. The best match is for 5.3×11 nm CdS nanorods and 5×5 nm Ag_2S nanocubes, which corresponds to the experimental nanorod diameters with an average center-to-center separation of 16 nm between Ag_2S segments. The Ag_2S peaks in the experimental data are broader than the computed ones, possibly due to strain created at the CdS-Ag_2S interfaces, which was not included in this calculation. The Ag_2S structure listed in Table 1 is similar to the previously reported structural data of bulk Ag_2S, but with slightly different Ag atoms positions.

Interface Formation Energy. During the initial stages of growth, when Ostwald ripening is dominant, the larger regions of Ag_2S absorb smaller islands. The direction of the process is determined by the interface formation energy, which is the energy difference between the CdS-Ag_2S interface and the corresponding Ag_2S and CdS bulk structures. A positive interface formation energy will result in Ostwald ripening, merging smaller islands into larger ones to a lower surface area, and thus

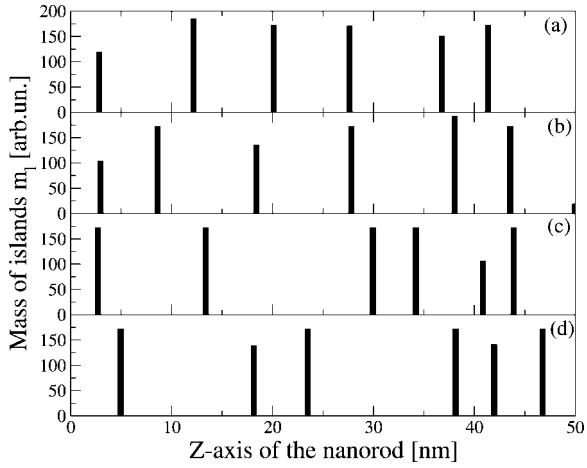

Figure 3. Results of the diffusion model for the ripening of islands in one-dimension. The islands are initially randomly formed in the one-dimensional rod. The growth of the larger islands at the expense of the smaller islands (*i.e.*, Ostwald ripening) leads to the formation of ordered islands due to diffusion. The length of the bars shows the relative number of Ag atoms in an island situated along the long axis of the nanorod (horizontal axis of the plot). The critical island size is $m_c = 100$. The panels a, b, c, and d show four different results of modeling for different initial random distributions of small islands. Diffusion alone produces somewhat ordered islands, but the ordering is typically poor. The results presented here are typical for diffusion-limited ordering. Panels a and b show relatively ordered patterns, while panels c and d are rather disordered; all patterns have similar probabilities of forming, showing overall poor ordering solely due to diffusion.

lowering the total energy. To clarify this, we calculated the CdS-Ag_2S interface formation energy for the supercell geometry constructed as in Figure 1c,d. The epitaxial attachments of (001) and (100) planes of Ag_2S to the CdS (0001) wurtzite plane were studied. Both attachments have almost the same lattice mismatch; however, because of the differences in elastic constants and chemical interface energies they have different formation energies. The CdS slab length was 19.4 Å and Ag_2S slabs were 15.88 and 15.78 Å, for the (001) and (100) attachments respectively, in the *z* -direction of the supercell, and infinite in the *xy* plane. The structures (both supercell and the bulk) were relaxed with respect to internal degrees of freedom, lattice parameters, and the distances between slabs. The interface formation energy computed from the *ab initio* total energies is given by

$$E_{\text{form}} = E_t - \sum_i N_i \mu_i \qquad (2)$$

Here, E_t is the total energy of the supercell, N_i is the number of atoms of the type *i* in the cell, and μ_i is the chemical potential of the *i*th atom. The supercell was large enough so the interaction between the two adjacent interfaces is negligible. Our first principles calculations result in a CdS-Ag_2S interface formation energies of +1.57 and +1.51 eV per primitive interface containing one Cd−S−Ag unit for epitaxial attachments of (100) and (001) planes. Note that this energy contains both the chemical formation energy and the elastic energy due to strain at the interface. The (001) attachment shown in Figure 1c,d has slightly lower formation energy. Owing to the large positive interface formation energies, it is energetically favorable to merge small islands into large ones. A critical size is reached when an island spans the entire nanorod diameter, forming an Ag_2S segment. In this case, exchange of cations between two fully formed segments does not decrease the Ag_2S segment surface area and surface energy.

Diffusion. Pattern formation in systems away from equilibrium has been extensively studied in the past.[25] In reaction-diffusion systems, a pattern can form because of a Turing instability: a solution which is stable and uniform in the absence of diffusion becomes unstable and produces a pattern when conditions are altered to allow diffusion.[26] During the formation of the CdS-Ag_2S nanorod superlattices, the reaction-diffusion system is out of equilibrium and results in periodic patterns with intrinsic wavelengths which are longer than (and consequently, dependent upon) the physical dimensions of the system, that is, the nanorod diameter. Within this viewpoint, the involvement of a Turing instability in the evolution of CdS-Ag_2S nanorod superlattice appears possible. However, the observed nucleation and ripening does not seem to be qualitatively consistent with a Turing instability. During a reaction displaying a Turing instability, the final pattern appears from the beginning, with its amplitude increasing with time. In the CdS-Ag_2S superlattices, however, assuming that the structures obtained at different Ag^+ concentrations also correspond to different stages in the evolution of the superlattices at a fixed concentration, islands appear to ripen and the segments appear to be mobile. In addition, the initial distribution of Ag_2S regions does not show periodicity (see Figure 3E in ref 15). Thus, the pattern of segments seems to change until a periodic spacing of islands is achieved, and therefore the observed ordering does not support a Turing model.

Spontaneous ordering on the nanoscale due to limited diffusion of adatoms has been studied in the past. Concerning 3D systems, several theories of kinetic ordering of islands have been proposed.[27] (Also see ref 8 and references therein). They may be adequate only at the initial stages of growth, since they ignore the influence of strain created by islands on the diffusion of atoms, which was pointed out to be important in 2D and 3D island growth.[28] The possibility of producing ordered patterns solely due to diffusion limited aggregation in 1D has been addressed theoretically,[14] where modeling the deposition of particles along a line results in regular patterns.

Here, we study this possibility in 1D by modeling the diffusion of Ag atoms between islands and the ripening of islands at the expense of each other. Initially, is-

lands of Ag_2S are randomly distributed along a 1D array, and are assigned random small sizes. Inside the CdS solid, there is a small number of free Ag atoms, which reach near-equilibrium with the Ag_2S islands. Islands can lose or gain Ag atoms from the CdS solid, and the direction of this process is defined by the energy balance described below.

We model the nanorod as an array of sites, here i is indexing all sites in the CdS host, while I is indexing islands, $i(I)$ is the site index of the Ith island. The energy cost to add one Ag atom to the Ith island located at the $i(I)$th site is approximated by the expression

$$\Delta E_I = -E_{Ag} + \beta m_I^{-1/3} - kT \ln\left[\frac{x_{i(I)}}{(1 - x_{i(I)})}\right] \qquad (3)$$

where, m_I is the number of atoms in the Ith island, $x_{i(I)}$ is the concentration of Ag atoms at the $i(I)$th site, E_{Ag} is the Ag_2S chemical formation energy (compared to free Ag atoms in CdS), and β is a constant that dictates the magnitude of the interfacial energy. The first term, $-E_{Ag}$ is negative, corresponding to the observation that the segregation of Ag^+ into Ag_2S islands appears to be favorable. The last term is the entropy of a mixture of Ag atoms in the CdS solid that depends on temperature, kT, and the Ag atom concentration x_i. If the energy, ΔE_I, is negative then it is favorable for the Ith island (at ith site) to absorb Ag atoms, if it is positive then this island will lose atoms. We also set the second term in eq 3 to zero after an island reaches some critical mass. For when the segment is fully formed, spanning the whole nanorod diameter, the exchange of atoms with the environment results in no change of the surface energy.

The model evolves with time according to the following three equations. The first two equations

$$x_{i(I)}(t+1) = x_{i(I)}(t) \pm \alpha x_{i(I)} e^{-\frac{E_b}{kT}} \qquad (4)$$

$$m_I(t+1) = m_I(t) \mp \alpha x_{i(I)} e^{-\frac{E_b}{kT}} \qquad (5)$$

describe the exchange of Ag atoms between the islands, m_I, and the CdS solid, x_i, at $i(I)$th site. Here the concentration of Ag atoms in the CdS solid, x_i, is increasing (*i.e.*, choosing $+$ sign in eq 4 and $-$ sign in eq 5) if ΔE_I is positive. This corresponds to an Ag_2S island losing atoms to the CdS, increasing its concentration by an amount proportional to α. We assume the energy activation barrier, E_b, to leave the island into the CdS matrix is independent of the island size, therefore adding a value proportional to Ag atom concentration $x_{i(I)}$ at a given temperature. The direction is reversed if ΔE_I is negative. The process is mediated by the diffusion of Ag atoms in the CdS defined by gradients of concentration x_i

$$x_i(t+1) = x_i(t) + D[x_{i+1}(t) + x_{i-1}(t) - 2x_i(t)] \qquad (6)$$

where D is the diffusion coefficient. The conservation of mass is enforced by limiting the diffusion direction at the boundaries toward the center of the rod. The parameters are chosen to model the experimental conditions and results, that is, formation of islands, ripening, and maintaining a low concentration of Ag in the CdS matrix. This is primarily achieved by choosing an optimal $\alpha/De^{-\{E_b/kT\}}$ ratio, which controls the diffusion and ripening rates. The term ΔE_I only indicates the direction of the ripening process for a given island, and its values are unimportant. The CdS solid and the islands reach thermodynamic quasi-equilibrium between islands and their surrounding x_i quite rapidly. Subsequently, the smaller islands slowly lose atoms to bigger islands, since the second term in eq 3 favors larger islands. Eventually, larger islands absorb the smaller islands entirely, modeling Ostwald ripening, and reach the critical size m_c, beyond which the segment is formed and the second term in eq 3 disappears.

Typical results of the modeling are shown in Figure 3, where we show the island weight and position on a typical 50 nm long nanorod. Initially, the islands were distributed randomly along the 1D nanorod and assigned small random sizes. The simulation then demonstrates behavior typical for Ostwald ripening, where larger islands grow at the expense of the smaller islands. The four panels show the resulting patterns after the Ostwald ripening is finished. All the islands have reached critical sizes where the energy balance will not change as a result of Ag exchange between islands. Figure 3, presenting a typical diffusion limited ordering scenario, shows that the islands are ordered poorly. Running a number of simulations for the geometry considered, even in somewhat ordered cases shown in panels a and b, there are always a few large islands located close to each other. In addition, equally probable are the cases where the ordering is very poor, as shown in Figure 3 panels c and d. Therefore, if spontaneous ordering were driven by diffusion alone, we would expect to observe experimentally rods with several out-of-place Ag_2S segments in practically every nanorod. In addition, a large number of fairly disordered nanorods would be expected. That, however, is not the case; experimentally, the Ag_2S segments are very well ordered (Figure 1a), indicating that diffusion-limited growth alone does not account for the formation of the CdS-Ag_2S nanorod superlattices. To produce such an ordered state, there must exist a repulsive interaction between the fully formed CdS-Ag_2S segments, which drives them apart. (The Ag_2S segments can shift their positions *via* exchange between Ag^+ and Cd^{2+} ions).

Strain. As established above, the nanorod superlattice formation mechanism, which results in a regular Ag_2S segment pattern, implies a repulsive interaction

between mobile segments. Among possible candidates for such interaction are (i) direct Coulomb repulsion, (ii) dipole–dipole interactions, and (iii) interaction due to strain. We address and discount the first two of these possibilities below.

(i) The Ag_2S segments exhibit photoluminescence (blue-shifted due to quantum confinement[15]), indicating that there are few dangling bond states in the band gap. This, along with TEM images and XRD data, indicate a well formed Ag_2S crystal, which is expected to be charge neutral. Therefore, direct Coulomb repulsion between Ag_2S segments is unlikely.

(ii) Dipole moments have been reported to be significant in wurtzite II−VI semiconductor nanocrystals in the past.[29,30] In addition, the ordering on the nanoscale due to the dipole–dipole interactions has been experimentally observed. For example, CdTe nanocrystals have been shown to self-assemble into nanowires due to the dipole–dipole interactions.[31] Similarly, PbSe nanocubes have been shown to order into chains, driven by the interactions of electric dipole moments.[32,33]

To estimate the possible dipole–dipole interaction, we have performed *ab initio* calculations for CdS-Ag_2S superlattices with alternating Ag_2S and CdS slabs in the *z*-direction and infinite cross section in *xy*-directions. We used 30 Å thick Ag_2S slabs (9 atomic layers) and the 42 Å thick slabs (12 atomic layers) of CdS. The lattice and the atoms in the three layers adjacent to the interfaces were relaxed. The results of the calculation give an electrostatic potential gradient inside the Ag_2S slabs of the superlattice, from which a dipole moment can be deduced. For an experimental nanorod of 4.8 nm diameter and Ag_2S segment of 3 nm length, it yields a dipole moment of approximately 290 Debye. If the symmetry of the lattice in the neighboring segments is the same, these dipole moments will point in the same direction. This interaction, first of all, cannot be used as an ordering mechanism, as it is attractive; second, its magnitude is very small (0.04 eV).

(iii) Due to a very large lattice mismatch, significant strain fields are created inside the nanorod. Therefore, the strain is a likely candidate for the repulsive interaction in CdS-Ag_2S nanorod superlattice. Using a VFF model and the elastic parameters, we explain and quantify this repulsive force between the Ag_2S segments.

To study the strain and elastic properties of the CdS-Ag_2S nanorod superlattices, we first calculate the elastic constants of the Ag_2S using *ab initio* methods. Although the orthorhombic supercell technically has nine independent elastic constants, in the case of the Ag_2S lattice attachment to wurtzite shown in Figure 1c,d, the distortions the Ag_2S lattice undergoes are mainly due to orthogonal uniaxial strain. Thus the shear elastic constants c_{44}, c_{55}, and c_{66} may be neglected in a basic treatment of the distortions, and therefore were not fitted. We only need the six remaining elastic constants c_{11}, c_{22}, c_{33}, c_{12}, c_{13}, and c_{23}. We relax the atomic structure of the Ag_2S unit, apply a small (within a few percent) strain δ_i to the equilibrium lattice and compute the resulting total energies (following ref 34). The total energy, assuming linear elasticity up to the limits of distortions, is fitted into a second order expansion in powers of strain tensor components around the equilibrium energy E_0:

TABLE 2. Elastic Constants c_{ij} (Using Voigt Notation) for the Orthorhombic Cell of Ag_2S in Units of [10^{11} dyne/cm^2] from First Principles GGA Calculations. We also List Experimental[35] Elastic Constants of CdS for Comparison

	reference	c_{11}	c_{22}	c_{33}	c_{12}	c_{13}	c_{23}
Ag_2S	present	8.02	9.76	11.57	2.59	3.49	4.36
CdS	experiment[35]	8.57		9.36	5.21	4.61	

$$E(\delta) = E_0 + \frac{1}{2}V_0\sum_{ij} c_{ij}\delta_i\delta_j + O[\delta^3] \quad (7)$$

where, V_0 is equilibrium volume. We need only consider the diagonal strain tensor **e** (with three diagonal components e_1, e_2, e_3), so we apply distortions to the primitive vectors a_i transforming them as

$$\begin{pmatrix} a'_1 \\ a'_2 \\ a'_3 \end{pmatrix} = \begin{pmatrix} a_1 \\ a_2 \\ a_3 \end{pmatrix} \cdot (\mathbf{I} + \mathbf{e}) \quad (8)$$

(**I** is the 3 × 3 identity matrix) fitting the total energy curves into eq7 and extracting the coefficients at the second order term. To find the elastic constants c_{11}, c_{22}, and c_{33}, three linear tetragonal distortions are applied to the lattice with the strain tensor components equaling, respectively,

$$e_1 = \delta_1,\ e_2 = e_3 = 0 \quad (9)$$

$$e_2 = \delta_2,\ e_1 = e_3 = 0 \quad (10)$$

and

$$e_3 = \delta_3,\ e_1 = e_2 = 0 \quad (11)$$

To find elastic constants c_{12}, c_{13}, and c_{23}, the orthorhombic strains are applied by using distortion matrices (**I** + **e**)γ and strain tensor components

$$e_1 = \delta_1,\ e_2 = -\delta_1,\ e_3 = 0,\ \gamma = (1-\delta_1^2)^{-1/3} \quad (12)$$

$$e_1 = \delta_2,\ e_2 = 0,\ e_3 = -\delta_2,\ \gamma = (1-\delta_2^2)^{-1/3} \quad (13)$$

and

$$e_1 = 0,\ e_2 = \delta_3,\ e_3 = -\delta_3,\ \gamma = (1-\delta_3^2)^{-1/3} \quad (14)$$

The resulting elastic constants are listed in the Table 2. We feed these bulk elastic constants into the VFF calcu -

TABLE 3. Introducing Asymmetry into the Ag_2S Segments Using VFF Calculations, the Elastic Energies, and Widths of Two Ag_2S Segments, with 4 nm Separation. The Growth of One Segment at the Expense of the Other is Energetically Unfavorable

segment 1	segment 2	energy
4 nm	4 nm	158.83 eV
3 nm	5 nm	159.25 eV
2 nm	6 nm	160.49 eV

lation for a nanostructure with a realistic number of atoms in order to study the influence of strain on the lattice mismatched nanorod superlattices.

The VFF model[36,37] is a classical atomistic model for atomic relaxation which treats atoms as points connected by elastic bonds and in our implementation[37] takes into account bond stretching and bond angle bending but not bond breaking. The VFF strain energy functional is written in terms of atomic positions R_i and their elastic interaction with the nearest neighbors only, within a harmonic approximation:

$$E = \frac{3}{16}\sum_i \left\{ \sum_j^{nn} \frac{\alpha_{ij}}{d_{ij}^2}[\Delta \mathbf{R}_{ij}^2 - d_{ij}^2]^2 + \sum_{j,k>j}^{nn} \frac{\beta_{ijk}}{d_{ij}d_{ik}}[\Delta \mathbf{R}_{ij} \cdot \Delta \mathbf{R}_{ik} - d_{ij}d_{ik}\cos\theta_{ijk}]^2 \right\} \quad (15)$$

where, $\Delta \mathbf{R}_{ij} = \mathbf{R}_j - \mathbf{R}_i$, d_{ij} is the ideal bond length between the i th and j th atom, θ_{ijk} is the ideal bond angle, and α_{ij} and β_{ijk} are the elastic constants of the model which are fitted to the elastic constants of the bulk Ag_2S and CdS. The summation over j and k indices is performed over nearest neighbors only, while the index i runs over all atoms in the nanostructure. The elastic constants α and β can be found from constants c_{ij},[37] computed from first principles for Ag_2S and fitted to experiment for CdS, and are (in units of [10^3 dyne/cm]) $\alpha = 29.60$ and $\beta = 9.23$ for Ag_2S, and $\alpha = 26.57$ and $\beta = 4.76$ for CdS. For a given nanostructure, the energy functional of eq 15 is minimized with respect to $\{\mathbf{R}_i\}$, yielding the atomic structure that has the lowest elastic energy for a given arrangement of atoms.

In the geometry studied here, the CdS-Ag_2S interface has lattice mismatches which are different in the x and y directions, as discussed above (Figure 1). Therefore, upon VFF relaxation, a nanorod will expand and contract along two perpendicular radial directions. We performed VFF calculations for CdS nanorod superlattices with diameters of 4.8 and 6 nm, which have two 4 nm thick Ag_2S segments at varying separations. The surfaces of the nanorods were passivated.[38] The rod lengths varied with the segment separation from 30 to 42 nm, keeping the distance between the segments and the nanorod ends constant in order to fix any possible contribution from the ends of the rods to the elastic energy. The number of atoms in the structures studied ranged from 25228 to 57201.

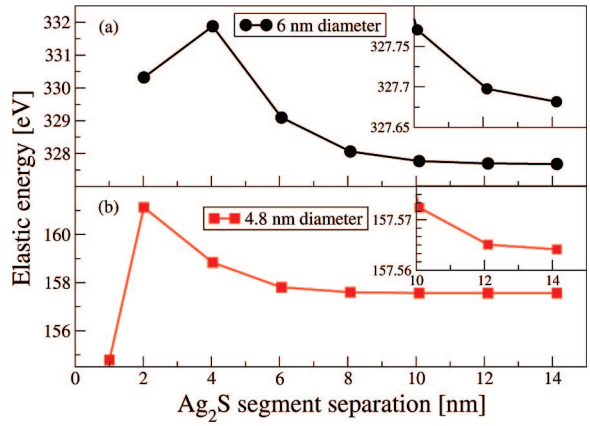

Figure 4. Elastic energies of CdS nanorod superlattices containing two Ag_2S segments calculated with the VFF model: (a) 6 nm diameter nanorod; (b) 4.8 nm diameter nanorod. The energies decay with growing separation showing the elastic interaction between Ag_2S segments.

The resulting elastic energies as functions of the segments separation are shown in Figure 4, for a 6 nm diameter nanorod (a) and a 4.8 nm diameter nanorod (b). The elastic energies decrease with increasing separation between the segments indicating elastic repulsion between the segments. The insets show blow-ups of the tail of the curves with the same x-axis scaling, showing exponential decay of the interaction energy. Owing to the increased interfacial area for larger diameter rods, the strain present in the 6 nm rods is greater than that in the 4.8 nm diameter rods, resulting in larger elastic energies. For very small separations, the elastic energy in Figure 4 is lowered, which will be explained when we examine the nature of the repulsive interaction (see below).

Strain fields, created by the lattice mismatch at the interface, decay both into the CdS regions and Ag_2S segments. Therefore, just as the elastic energy decreases with the length of the CdS regions separating the two CdS-Ag_2S interfaces, it also decreases with increasing Ag_2S segment size. For a given number of segments, the elastic energy is minimized when the size of all CdS regions is maximal, and the adjacent Ag_2S segments are equidistant from each other. Similarly, when the Ag_2S segments also have equal sizes, this maximizes the separations between CdS-Ag_2S interfaces within the segments. Indeed, introducing asymmetry into the Ag_2S segment widths results in higher elastic energies. For instance, the results of VFF calculations for the 4.8 nm diameter rods, with two asymmetric Ag_2S segments are presented in Table 2. This indicates that the diffusion of Ag^+ ions and growth of one fully formed segment at the expense of another is energetically unfavorable. The lowest elastic energy is reached when all the segments in the nanorod have the same width. This is consistent with the experimental finding of spontaneous ordering of Ag_2S segments,

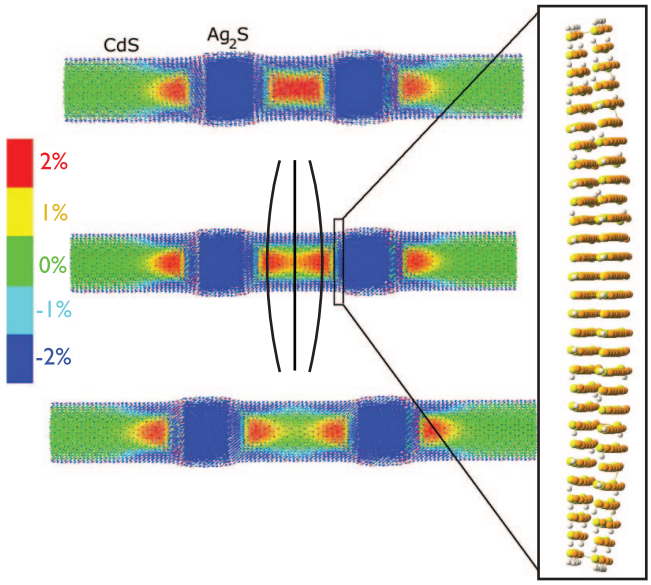

Figure 5. Color maps of the *z*-component of strain in the interatomic bonds, for the 4.8 nm diameter nanorod. The segment separations are 6, 8, and 10 nm. The color map limits indicate a strain of −2% (compression) to +2% (tension) for blue and red, respectively. The blow-up on the right shows two layers of CdS adjacent to the Ag_2S segment, illustrating CdS planes acquiring a convex shape. The atoms are pulled in opposite directions (indicated by the black lines at the center of the second rod), which leads to an increased interaction energy when the segments separation decreases.

as well as the narrow distribution of Ag_2S segment widths.[15]

It should be noted that the resulting superlattice is a metastable structure. The lowest energy structure would consist of only two regions, Ag_2S and CdS with a single interface, as this would minimize both the interface formation and strain energies. However, such state cannot be reached because once a segment is fully formed, diffusion of Ag^+ ions will not lower the interfacial energy until the two segments fully merge. That, in turn, is unfavorable because of the repulsion between segments due to strain. The elastic repulsion, preventing the two segments merging defines the energy barrier between the metastable state and the equilibrium state. Therefore, for example, for 6 nm diameter rods, this barrier can be estimated as 4.2 eV per a pair of segments (see Figure 4). On a per interface basis, this energy is comparable to thermal fluctuations at reaction temperature. Note however, that this barrier represents only the equilibrium difference in energy for nanorods with Ag_2S segments placed at increasingly smaller separations. The kinetic barrier for moving cations to merge the segments may be considerably higher. Although for a given pair of segments the strain repulsion energy is about 2 orders of magnitude lower than the interface formation energy, they both play important roles at different stages of formation. The initial nucleation and islands growth is driven primarily by the tendency to lower the interface formation energy. However the final ordering and segments stabilization is determined by the strain interactions, when the formation energy is minimal and constant for a given number of segments.

To illustrate the elastic interaction between the two segments, we plot color-coded maps of the *z* -component of the bond strain for the 4.8 nm diameter nanorod with segment separations of 6, 8, and 10 nm, in Figure 5. The VFF relaxation predicts the 3D strain field resulting from the lattice mismatch at the interface. Although the full strain is a tensor field, the interaction can be demonstrated by looking at the *z*-axis strain fields. The overlap of *z*-strain is greater for smaller Ag_2S segment separation. The red regions between the segments decay away from the segment indicating that the interatomic bonds are stretched in the *z*-direction, with such distortion increasing toward the central axis of the rod. This results in an overall deformation of CdS interatomic layers in the *xy* plane from flat to convex, as demonstrated by a two layer CdS cutout in Figure 5. Since the *xy* plane in the middle between the convex regions must be flat, the deformations exemplified by the curved planes create competing forces, as schematically shown in Figure 5, resulting in a repulsive interaction.

This model also explains why for small separations between Ag_2S segments, that is, below 4 nm for 6 nm diameter rods, and below 2 nm for 4.8 diameter rods the elastic energy actually decreases (Figure 4). This is due to the fact that strains in *z*-direction created by the two neighboring segments are the result of bonds stretched in opposite directions. However, in the $x-y$ direction stretching from the two segments match each other, for small segment separations. This cooperation lowers the strain energy and leads to an energy decrease at small segment separations as shown in Figure 4.

It is important to note that our VFF calculations for a variety of lattice mismatched hybrid nanorod structures indicate that such strain-mediated repulsive interaction is a general effect. For a given pair of lattice mismatched materials, it is always present in nanostructures, resulting in energy curves similar to the ones in Figure 4. This should play an important part in the formation of lattice mismatched hybrid nanostructures.

CONCLUSIONS

In this work, we have performed an analysis of the structural and elastic properties of recently synthesized CdS-Ag_2S nanorod superlattices. Using experimental XRD data, we deduce the lattice geometry for the epitaxial attachment of monoclinic Ag_2S and wurtzite CdS. Using first principles methods, we calculated the formation energy of the CdS-Ag_2S interface, which indicates Ostwald ripening during the initial stages of Ag_2S nucleation and growth. A simple model of Ag^+ diffusion shows that the Ag_2S islands will condense into a number of segments, rather than divide a rod into two (or a few) large segre-

gated sections of Ag_2S and CdS. This model also shows that diffusion-limited growth of the Ag_2S islands can only lead to partial ordering and cannot account for the observed periodic structures alone. The epitaxial attachment of Ag_2S and CdS in the nanorod leads to significant amounts of strain due to a substantial lattice mismatch. Our VFF calculations show that this results in elastic repulsion between neighboring Ag_2S segments. This interaction due to strain is crucial to the formation of nanorod superlattices since it can lead to spontaneous ordering of Ag_2S segments. This should be a general effect in the evolution of epitaxially connected nanocrystal nanostructures, that is, similar repulsive interactions will always exist wherever there is a mismatch between components in a hybrid nanostructure. The effect of strain interactions is also important for stabilizing the structure, since such a superlattice is a metastable state against a completely segregated phase.

METHODS

The experimental procedure for fabricating CdS-Ag_2S nanorod superlattices has been published elsewhere.[15] An image of the nanostructures modeled here is shown in Figure 1a, where segments of Ag_2S have spontaneously formed within CdS nanorods in a periodic arrangement. To theoretically clarify the formation mechanism and properties of these structures, we use a combination of *ab initio* methods as well as the classical valence force field (VFF) method. The first principles calculations of the elastic properties of Ag_2S and CdS-Ag_2S interfaces and superlattices employed the VASP,[39] and Petot packages.[40] We used the generalized gradient (GGA) as well as local density (LDA) approximations, along with projector augmented wave (PAW) and norm-conserving pseudopotential methods. To study the role that diffusion-limited island growth plays in producing the observed ordering, we employ a simple kinetic model in 1D, which describes Ostwald ripening due to diffusion of atoms between the islands. The VFF model[36] was used to compute the lattice strain fields in the experimental size nanorod superlattices, with parameters obtained from fitting the Ag_2S elastic constants obtained from the first principles calculations.

Acknowledgment. This work was supported by U.S. Department of Energy under Contract No. DE-AC02-05CH11231 and used the resources of the National Energy Research Scientific Computing Center (NERSC).

REFERENCES AND NOTES

1. Wu, Y.; Fan, R.; Yang, P. Block-by-Block Growth of Single-Crystalline Si/SiGe Superlattice Nanowires. *Nano Lett.* **2002**, *2*, 83–86.
2. Björk, M. T.; Ohlsson, B. J.; Sass, T.; Persson, A. I.; Thelander, C.; Magnusson, M. H.; Deppert, K.; Wallenberg, L. R.; Samuelson, L. One-Dimensional Steeplechase for Electrons Realized. *Nano Lett.* **2002**, *2*, 87–89.
3. Gudiksen, M. S.; Lauhon, L. J.; Wang, J.; Smith, D. C.; Lieber, C. M. Growth of Nanowire Superlattice Structures for Nanoscale Photonics and Electronics. *Nature* **2002**, *415*, 617–620.
4. Achermann, M.; Petruska, M. A.; Kos, S.; Smith, D. L.; Koleske, D. D.; Klimov, V. I. Energy-Transfer Pumping of Semiconductor Nanocrystals Using an Epitaxial Quantum Well. *Nature* **2004**, *429*, 642–646.
5. Gur, I.; Fromer, N. A.; Geier, M. L.; Alivisatos, A. P. Air-Stable All-Inorganic Nanocrystal Solar Cells Processed from Solution. *Science* **2005**, *310*, 462–465.
6. Milliron, D. J.; Hughes, S. M.; Cui, Y.; Manna, L.; Li, J.; Wang, L.-W.; Alivisatos, A. P. Colloidal Nanocrystal Heterostructures with Linear and Branched Topology. *Nature* **2004**, *430*, 190–195.
7. Ouyang, L.; Maher, K. N.; Yu, C. L.; McCarty, J.; Park, H. Catalyst-Assisted Solution-Liquid-Solid Synthesis of CdS/CdSe Nanorod Heterostructures. *J. Am. Chem. Soc.* **2007**, *129*, 133–138.
8. Shchukin, V. A.; Bimberg, D. Spontaneous Ordering of Nanostructures on Crystal Surfaces. *Rev. Mod. Phys.* **1999**, *71*, 1125–1171.
9. Nötzel, R. Self-Organized Growth of Quantum-Dot Structures. *Semicond. Sci. Technol.* **1996**, *11*, 1365–1379.
10. Miller, M. S.; Malm, J.-O.; Pistol, M.-E.; Jeppesen, S.; Kowalski, B.; Georgsson, K.; Samuelson, L. Stacking InAs Islands and GaAs Layers: Strongly Modulated One Dimensional Electronic System. *J. Appl. Phys.* **1996**, *80*, 336–33640.
11. Capellini, G.; Seta, M. D.; Evangelisti, F.; Zinovyev, V. A.; Vastola, G.; Montalenti, F.; Miglio, L. Self-Ordering of a Ge Island Single Layer Induced by Si Overgrowth. *Phys. Rev. Lett.* **2006**, *96*, 106102–106106.
12. Xie, Q.; Madhukar, A.; Chen, P.; Kobayashi, N. P. Vertically Self-Organized InAs Quantum Box Islands on GaAs(100). *Phys. Rev. Lett.* **1995**, *75*, 2542–2545.
13. Tersoff, J.; Teichert, C.; Lagally, M. G. Self-Organization in Growth of Quantum Dot Superlattices. *Phys. Rev. Lett.* **1996**, *77*, 1675–1678.
14. Vicsek, T. Pattern Formation in Diffusion-Limited Aggregation. *Phys. Rev. Lett.* **1984**, *53*, 2281–2284.
15. Robinson, R. D.; Sadtler, B.; Demchenko, D. O.; Erdonmez, C. K.; Wang, L.-W.; Alivisatos, A. P. Spontaneous Superlattice Formation in Nanorods through Partial Cation Exchange. *Science* **2007**, *317*, 355–358.
16. Son, D. H.; Hughes, S. M.; Yin, Y.; Alivisatos, A. P. Cation Exchange Reactions in Ionic Nanocrystals. *Science* **2004**, *306*, 1009–1012.
17. Chan, E. M.; Marcus, M. A.; Fakra, S.; ElNaggar, M.; Mathies, R. A.; Alivisatos, A. P. Millisecond Kinetics of Nanocrystal Cation Exchange Using Microfluidic X-ray Absorption Spectroscopy. *J. Phys. Chem. A* **2007**, *111*, 12210−12215.
18. Dzhafarov, T. D.; Serin, M; Ören, D.; Süngü, B.; Sadigov, M. S. The Effect of Ag Photodiffusion on Characteristics of Ag-CdS Diode Structures. *J. Phys. D: Appl. Phys.* **1999**, *32*, L5–L8.
19. Woodbury, H. H. Diffusion of Cd in CdS. *Phys. Rev.* **1964**, *134*, A492–A498.
20. Schmalzried, H. Ag_2S−The Physical Chemistry of an Inorganic Material. *Prog. Solid State Chem.* **1980**, *13*, 119–157.
21. Kashida, S.; Watanabe, N.; Hasegawa, T.; Iida, H.; Mori, M.; Savrasov, S. Electronic Structure of Ag_2S, Band Calculation and Photoemission Spectroscopy. *Solid State Ionics* **2003**, *158*, 167–175.
22. Junod, P.; Hediger, H.; Kilchör, B.; Wullschleger, J. Metal-non-Metal Transition in Silver Chalcogenides. *Philos. Mag.* **1977**, *36*, 941–958.
23. Kästner, G.; Gösele, U. Stress and Dislocations at Cross-Sectional Heterojunctions in a Cylindrical Nanowire. *Philos. Mag.* **2004**, *84*, 3803–3824.
24. Ertekin, E.; Greaney, P. A.; Chrzan, D. C.; Sands, T. D. Equilibrium Limits of Coherency in Strained Nanowire Heterostructures. *J. Appl. Phys.* **2005**, *97*, 114325–114335.
25. Cross, M. C.; Hohenberg, P. C. Pattern Formation Outside of Equilibrium. *Rev. Mod. Phys.* **1993**, *65*, 851–1112.
26. Castets, V.; Dulos, E.; Boissonade, J.; Kepper, P. D. Experimental Evidence of a Sustained Standing Turing-type Nonequilibrium Chemical Pattern. *Phys. Rev. Lett.* **1990**, *64*, 2953–2956.
27. Dobbs, H. T.; Vvedensky, D. D.; Zangwill, A.; Johansson, J.; Carlsson, N.; Seifert, W. Mean-Field Theory of Quantum Dot Formation. *Phys. Rev. Lett.* **1997**, *79*, 897–900.

28. Chen, Y.; Washburn, J. Structural Transition in Large-Lattice-Mismatch Heteroepitaxy. *Phys. Rev. Lett.* **1996**, *77*, 4046–4049.
29. Shim, M; Guyot-Sionnest, P. Permanent Dipole Moment and Charges in Colloidal Semiconductor Quantum Dots. *J. Chem. Phys.* **1999**, *111*, 6955–z6964.
30. Li, L.; Alivisatos, A. P. Origin and Scaling of the Permanent Dipole Moment in CdSe Nanorods. *Phys. Rev. Lett.* **2003**, *90*, 097402–097405.
31. Tang, Z.; Kotov, N. A.; Giersig, M. Spontaneous Organization of Single CdTe Nanoparticles into Luminescent Nanowires. *Science* **2002**, *297*, 237–240.
32. Cho, K.-S.; Talapin, D. V.; Gaschler, W.; Murray, C. B. Designing PbSe Nanowires and Nanorings through Oriented Attachment of Nanoparticles. *J. Am. Chem. Soc.* **2005**, *127*, 7140–7147.
33. Zhang, X.; Zhang, Z.; Glotzer, S. C. Simulation Study of Dipole-Induced Self-Assembly of Nanocubes. *J. Phys. Chem. C* **2007**, *111*, 4132–4137.
34. Ravindran, P.; Fast, L.; Korzhavyi, P. A.; Johansson, B.; Wills, J.; Eriksson, O. Density Functional Theory for Calculation of Elastic Properties of Orthorhombic Crystals: Application to $TiSi_2$. *J. Appl. Phys.* **1998**, *84*, 4891–4904.
35. Corll, J. A. Effect of Pressure on the Elastic Parameters and Structure of CdS. *Phys. Rev.* **1967**, *157*, 623–626.
36. Williamson, A.; Wang, L.; Zunger, A. Theoretical Interpretation of the Experimental Electronic Structure of Lens-Shaped Self-Assembled InAs/GaAs Quantum Dots. *Phys. Rev. B* **2000**, *62*, 12963–12977.
37. Pryor, C.; Kim, J.; Wang, L. W.; Williamson, A. J.; Zunger, A. Comparison of Two Methods for Describing the Strain Profiles in Quantum Dots. *J. Appl. Phys.* **1997**, *83*, 2548–2554.
38. Wang, L. W.; Li, J. First Principle Thousand Atom Quantum Dot Calculations. *Phys. Rev. B* **2004**, *69*, 153302–153306.
39. Kresse, G.; Furthmüller, J. Efficiency of Ab-Initio Total Energy Calculations for Metals and Semiconductors Using a Plane-Wave Basis Set. *Comput. Mater. Sci.* **1996**, *6*, 15–50.
40. Wang, L.-W. PEtot (parallel total energy) Density Functional Code. http://hpcrd.lbl.gov/linwang/PEtot/PEtot.html.